

WATER MASER MOTIONS IN W3(OH) AND A DETERMINATION OF ITS DISTANCE

K. HACHISUKA,^{1,2} A. BRUNTHALER,^{1,3} K. M. MENTEN,¹ M. J. REID,⁴ H. IMAI,⁵
Y. HAGIWARA,^{6,7} M. MIYOSHI,⁶ S. HORIUCHI,⁸ AND T. SASAO⁹

Received 2005 September 15; accepted 2006 January 24

ABSTRACT

We report phase-referencing VLBA observations of H₂O masers near the star-forming region W3(OH) to measure their parallax and absolute proper motions. The measured annual parallax is 0.489 ± 0.017 mas (2.04 ± 0.07 kpc), where the error is dominated by a systematic atmospheric contribution. This distance is consistent with photometric distances from previous observations and with the distance determined from CH₃OH maser astrometry presented in a related paper. We also find that the source driving the H₂O outflow, the “TW-object,” moves with a three-dimensional velocity of >7 km s⁻¹ relative to the ultracompact H II region W3(OH).

Subject headings: astrometry — masers — stars: distances — stars: formation — stars: individual (W3(OH)) — stellar dynamics

Online material: color figures

1. INTRODUCTION

The annual parallax is the most direct measurement of distances in astronomy. The *Hipparcos* satellite successfully measured the distances to numerous stars in the solar neighborhood, typically achieving 10% accuracies for distances of ≈ 100 pc, which contributed significantly to many fields of modern astronomy (e.g., Perryman et al. 1995). However, annual parallax measurements for stars with kiloparsec distances require submilliarcsecond accuracy, which has not been achieved optically.

Very long baseline interferometry (VLBI) provides the highest resolution in astronomy. In phase-referencing VLBI, the position of a target source is measured relative to a nearby positional reference source (see, e.g., Beasley & Conway 1995; Ros 2005). The feasibility of annual parallax measurements with the Very Long Baseline Array (VLBA) has been demonstrated at low frequencies by Brisken et al. (2002), who measured annual parallaxes of pulsars in the Galaxy, and by van Langevelde et al. (2000) and Vlemmings et al. (2003), who measured distances of Galactic OH masers associated with late-type stars. Chatterjee et al. (2004) measured pulsar parallaxes at 5 GHz and showed that the accuracy of astrometric measurements improves with higher frequencies. Their results indicate that one can measure distances of up to a few kpc with better than 10% uncertainty with VLBA astrometry of maser sources. Indeed, Kurayama et al. (2005) used the VLBA to measure the annual parallax of the Mira-type star UX Cygni with high accuracy.

Hence, VLBA measurements allow sources spread over a large part of the Milky Way to have accurate parallaxes. This enables us to probe Galactic structure and dynamics since maser sources are spread over the whole Galaxy; especially water vapor (H₂O) maser sources are even found in its outer reaches (e.g., Wouterloot et al. 1993).

The 22.2 GHz transition of H₂O is the most widespread and luminous known maser line. In our Galaxy it has been detected toward numerous evolved red giant stars and high- and low-mass star-forming regions (see, e.g., Valdetaro et al. 2001).

W3(OH) is a region containing several high- and intermediate-mass young stars and protostars of different evolutionary stages (e.g., Wilner et al. 1999; Wyrowski et al. 1997, 1999). In addition to strong OH and CH₃OH masers, which are seen projected on the archetypal ultracompact (UC) H II region, very strong H₂O maser emission is found toward the Turner-Welch (TW) object (Turner & Welch 1984; Reid et al. 1995; Wilner et al. 1999), a protostar projected $\approx 10^4$ AU east of the UC H II region. The W3(OH) H₂O masers were among the first studied with VLBI (Moran et al. 1973). VLBI maps of the H₂O maser emission have been reported by Alcolea et al. (1993).

We observed W3(OH) to measure its annual parallax and to study the internal dynamics of the known bipolar H₂O outflow from the TW object. Moreover, our observations constitute a trial parallax and proper motion observation to explore the potential of utilizing H₂O masers as probes of Galactic structure. Here we report VLBA observations of the W3(OH) H₂O masers that yielded an extremely accurate parallax.

2. OBSERVATIONS AND DATA REDUCTION

We observed the W3(OH) H₂O masers seven times with the NRAO VLBA¹⁰ between 2001 January and 2002 May (see Table 1). Each observation was carried out over a 4 hr period including calibrator observations. The separations between the epochs were between 2 and 4 months. We observed two 16 MHz bands with one band centered on the maser velocity. The data

¹ Max-Planck-Institut für Radioastronomie, Auf dem Hügel 69, 53121 Bonn, Germany.

² Departament de Astronomia, Universitat de València, Burjassot, Valencia 46100, Spain.

³ Joint Institute for VLBI in Europe, Postbus 2, 7990 AA Dwingeloo, Netherlands.

⁴ Harvard Smithsonian Center for Astrophysics, 60 Garden Street, Cambridge, MA 02138.

⁵ Department of Physics, Kagoshima University, Kagoshima 890-0065, Japan.

⁶ National Astronomical Observatory, Mitaka, Tokyo 181-8588, Japan.

⁷ ASTRON, Westerbork Observatory, P.O. Box 2, 7990 AA Dwingeloo, Netherlands.

⁸ Centre for Astrophysics and Supercomputing, Swinburne University of Technology, P.O. Box 218, Hawthorn, VIC 3122, Australia.

⁹ Department of Space Survey and Information Technology, Ajou University, Suwon 442-749, South Korea.

¹⁰ The VLBA is operated by the National Radio Astronomy Observatory (NRAO). The National Radio Astronomy Observatory is a facility of the National Science Foundation operated under cooperative agreement by Associated Universities, Inc.

TABLE 1
SUMMARY OF THE VLBA OBSERVATIONS

Epoch (UT)	Stations
2001 Jan 28, 01:11:00–05:13:00	7
2001 May 12, 18:20:00–22:20:00	9
2001 Jul 12, 14:20:00–18:20:00	8
2001 Aug 25, 11:27:00–15:27:00	9
2001 Oct 23, 07:35:00–11:35:00	9
2002 Jan 12, 02:16:00–06:16:00	9
2002 May 6, 18:44:00–22:44:00	7

were correlated with 1024 spectral channels in each band with an integration time of 2 s. The resulting velocity channel spacing was 0.224 km s^{-1} , and we covered a velocity range of 229 km s^{-1} .

We used ICRF 0244+624 as a phase-reference source. Its angular separation from W3(OH) is 2.2° . Since this source is extragalactic with a redshift of 0.0438 (Margon & Kwitter 1978), its proper motion should be negligible. The source was detected at all epochs with peak flux densities $>0.9 \text{ Jy}$. The source was compact and unresolved as in previous VLBI observations at lower frequencies (Fey & Charlot 2000), making it an excellent phase-reference source. Typical source elevations varied from 46° to 62° . We switched every 20 s between the sources W3(OH) and ICRF 0244+624, yielding typical on-source times of 7 s. The strong source NRAO 150 was observed for 5 minutes every 44 minutes for delay and bandpass calibration.

The data were calibrated and imaged with standard techniques using the NRAO Astronomical Image Processing System (AIPS) software package. Amplitude calibration used system temperature measurements and standard gain curves. A fringe fit was performed on ICRF 0244+624, and the solutions were applied to W3(OH). The Kitt Peak and Los Alamos antennas did not observe in the first epoch because of heavy snow; the Pie Town antenna was flagged in the third and seventh epochs since most of the data was lost because of system failures. Also, the Saint Croix antenna was flagged in all epochs as it produced little useful data, probably owing to its moist, low-latitude, low-elevation site and the absence of short baselines to this telescope.

Given an accurate geometric model in the VLBA correlator, the largest errors in phase-referencing observations are introduced by a zenith delay error in the atmospheric model of the correlator (see Reid et al. 1999). These errors degrade the image quality and the astrometric accuracy. The main contributions to the fringe phase of the target source, after phase-referencing, are from a position offset and the atmospheric/ionospheric delay error (if the source structure is negligible). Because of the different behavior of the two contributions, it is possible to separate both effects and to estimate the position offset as well as a zenith delay error. We fit a model phase owing to a position offset and a zenith delay error at each station to the calibrated phase data of an isolated and strong maser feature. The phase errors caused by the zenith delay errors can then be corrected by the AIPS task CLCOR. This correction improves the quality of the phase-referenced images and the astrometric accuracy (Reid et al. 1999; Reid & Brunthaler 2004; Brunthaler et al. 2005). The data from the Mauna Kea antenna at the seventh epoch were flagged, since we could not accurately estimate the zenith delay error of this station. After applying these corrections to the UV data of W3(OH), we created images of the maser features for each epoch.

We determined the position of each maser spot by fitting a two-dimensional Gaussian brightness distribution to the maps,

using the AIPS task JMFIT. The *formal* errors of the positions were calculated from the signal-to-noise ratio of the fitted peak flux densities and sizes of the components and were typically $10 \mu\text{as}$ in right ascension and $20 \mu\text{as}$ in declination.

3. RESULTS

We found a total of 42 distinct H_2O maser features that were detectable over three epochs, usually in 2 to 10 adjacent velocity channels with peak flux densities from a few hundred mJy to a few hundred Jy (Table 2). The masers were distributed over an area of $2.5'' \times 0.5''$ (Fig. 1), which is consistent with previous VLBI observations (Alcolea et al. 1993).

The absolute proper motion of a maser feature is the sum of the outflow motion in W3(OH), annual parallax, Galactic rotation, solar motion, and peculiar motion of W3(OH). We assumed all motions except the annual parallax to be linear. All motions, except the internal motions, are equal for all maser features. It can be challenging to trace exactly the same maser feature, since H_2O masers are highly time-variable and their absolute proper motions relative to the extragalactic reference source are nonlinear because of the effect of the parallax. For the feature identification we used not the absolute proper motions but the motions relative to a reference feature (feature 1 in Table 2) and then looked for rectilinear motions of a reasonable magnitude (i.e., $<100 \text{ km s}^{-1}$) in each spectral channel. The relative motions in Table 2 were obtained after a phase self-calibration on the reference feature to reduce systematic errors.

3.1. The Annual Parallax of W3(OH)

Once we identified a maser feature over five or more epochs, we modeled its path in terms of its proper motion (μ_α , μ_δ) and the annual parallax (Π) by using

$$\Delta\alpha \cos \delta = \Pi f_\alpha(\alpha, \delta, t) + \mu_\alpha t + \alpha_0, \quad (1)$$

$$\Delta\delta = \Pi f_\delta(\alpha, \delta, t) + \mu_\delta t + \delta_0, \quad (2)$$

where t is time, α_0 and δ_0 are the positions of a maser feature at $t = 0$, and the functions f_α and f_δ are the parallax displacements in right ascension and declination, respectively, given for example by Smart (1965, p. 221).

First, we fitted a proper motion and an annual parallax to all velocity channels individually. The reduced χ^2 values of the fits were very high (10–20). This was caused by unrealistically small formal errors of the position estimates, especially for strong sources. Hence, we introduced an error floor by adding quadratically a value of 0.05 mas to the formal position error. Possible sources of the error floor are variation of the centroid position of extragalactic source, residual errors in the estimation of zenith delay corrections, and blending of maser features. This resulted in a reduced χ^2 near unity. Thus, the positional accuracy of a single channel in a single epoch is $\sim 50 \mu\text{as}$.

It is very difficult to quantify the individual error contributions. The variations in the centroid position of the extragalactic reference source can be caused by unresolved structure changes and could be a few tens of microarcseconds per year. This motion should not influence the parallax measurement, if the motion is constant over the time of our experiment. However, in the case of an ejection of a new jet component, one could get nonlinear motions that affect the parallax measurements. This cannot be excluded since we did not use a second extragalactic reference source in our observations. However, ejections of new jet components are usually accompanied by sharp rises in the flux

TABLE 2
DETECTED H₂O MASERS

NUMBER	OFFSET ^a (mas)		EPOCHS	RELATIVE PROPER MOTION ^b (mas yr ⁻¹)				V_{LSR}^c (km s ⁻¹)		PEAK FLUX ^d (Jy beam ⁻¹)	
	E-W	N-S		E-W	Error	N-S	Error	Max	Min	Max	Min
1.....	-144.49	-144.29	7	0	±0	0	±0	-50.9	-51.3	304.6	57.7
2.....	2.33	6.27	6	0.62	0.13	2.30	0.18	-47.9	-48.8	95.8	12.4
3.....	1.97	6.52	5	0.54	0.28	2.63	0.19	-47.9	-48.2	165.5	33.3
4.....	-4.92	-5.68	7	1.06	0.06	1.26	0.09	-48.2	-48.8	335.5	65.4
5.....	-9.45	3.00	4	0.97	0.14	1.41	0.19	-48.2	-48.6	253.1	21.6
6.....	-9.63	33.42	7	0.37	0.06	2.73	0.05	-48.4	-49.0	367.0	40.5
7.....	-8.22	33.69	6	0.87	0.11	2.57	0.11	-48.6	-49.6	127.0	12.6
8.....	-6.38	33.18	5	-0.15	0.11	3.06	0.07	-49.8	-49.8	12.9	5.5
9.....	-4.83	32.42	4	0.66	0.58	2.88	0.18	-49.6	-49.8	20.6	4.9
10.....	-19.26	39.29	4	-0.17	0.17	2.81	0.13	-48.8	-49.4	72.3	9.9
11.....	-13.67	49.22	5	0.83	0.08	1.51	0.20	-49.2	-49.6	255.2	21.9
12.....	-21.64	63.22	6	1.09	0.29	1.02	0.18	-49.0	-49.2	126.1	51.9
13.....	-20.30	62.46	5	0.42	0.15	2.16	0.09	-48.8	-49.0	170.1	49.1
14.....	-21.95	64.34	4	0.40	0.31	2.20	0.62	-49.0	-49.2	77.8	18.1
15.....	-26.84	75.60	5	0.47	0.07	1.84	0.20	-48.4	-48.4	55.2	9.7
16.....	-38.68	98.35	6	0.01	0.09	2.01	0.04	-49.6	-49.6	102.4	14.5
17.....	-643.08	90.22	6	0.08	0.23	1.49	0.08	-51.1	-51.5	41.8	8.8
18.....	-648.91	91.76	3	2.95	0.10	1.82	0.13	-53.0	-53.2	9.7	5.7
19.....	-650.25	92.27	5	1.86	0.34	1.94	0.39	-52.6	-51.7	10.4	3.7
20.....	-650.64	92.11	5	0.73	0.10	1.43	0.10	-52.6	-52.8	35.7	3.7
21.....	-663.46	95.49	6	0.47	0.08	1.40	0.06	-54.3	-54.7	22.5	3.2
22.....	-674.24	96.97	3	3.96	0.27	1.11	0.14	-55.1	-55.1	7.7	3.1
23.....	-673.21	96.43	3	4.59	0.30	1.04	0.41	-54.9	-55.1	2.1	1.4
24.....	-680.99	95.14	4	0.07	0.09	1.51	0.10	-55.7	-56.0	6.6	1.0
25.....	-758.57	-48.82	3	6.86	0.07	-3.12	0.15	-59.5	-60.2	3.5	0.6
26.....	-826.70	-38.99	3	3.40	0.04	-0.80	0.01	-57.2	-57.2	7.2	2.6
27.....	-827.14	-38.23	5	3.75	0.14	-0.53	0.06	-57.4	-57.6	2.6	0.9
28.....	-831.22	-35.39	3	1.26	1.04	-0.70	0.01	-56.8	-57.4	3.2	1.6
29.....	-863.41	-12.12	5	2.58	0.23	-0.03	0.12	-58.5	-60.2	30.0	1.0
30.....	-942.98	1.95	3	-4.60	0.34	-0.18	0.71	-64.6	-65.0	0.6	0.2
31.....	-963.36	59.78	3	-4.01	0.99	4.00	0.15	-51.9	-52.4	32.9	18.6
32.....	-964.18	60.34	3	-3.28	0.24	3.07	0.64	-51.7	-51.9	57.2	12.9
33.....	-975.72	54.48	5	-5.02	0.14	3.01	0.13	-59.1	-60.8	2.0	0.8
34.....	-976.17	54.40	6	-4.77	0.37	3.31	0.10	-59.5	-61.2	2.6	0.9
35.....	-982.77	80.99	3	-1.44	0.14	1.19	0.10	-53.6	-54.1	283.8	121.9
36.....	-983.46	81.71	3	-0.06	0.06	-3.85	0.11	-53.4	-53.6	658.0	230.5
37.....	-983.47	82.56	4	-1.14	0.08	0.81	0.33	-53.0	-53.4	70.5	9.3
38.....	-985.41	-24.01	3	-3.86	0.04	0.82	0.07	-53.8	-54.1	97.7	52.0
39.....	-988.70	75.89	4	-2.91	0.09	2.81	0.08	-61.4	-61.8	3.5	0.6
40.....	-1034.87	-34.44	3	-3.20	0.05	0.26	0.13	-57.8	-58.1	6.5	2.1
41.....	-2045.95	-133.41	7	-1.93	0.06	1.36	0.09	-45.2	-45.2	28.7	7.8
42.....	-2231.40	84.12	6	-3.48	0.16	0.67	0.17	-62.5	-63.1	121.1	4.3

^a Origin of position offsets is $\alpha_{J2000} = 2^{\text{h}}27^{\text{m}}04^{\text{s}}8362 \pm 0^{\text{s}}0004$, $\delta_{J2000} = 61^{\circ}52'24''607 \pm 0''002$.

^b Motion of strongest channel relative to the reference feature 1. Errors are normalized for χ^2 .

^c Time variation of the LSR velocity in the channel with the highest peak flux. The velocity drift is constant for some H₂O masers, while it is fluctuating within listed velocities for others. This is most likely caused by blending with the intensities of blended features changing relative to each other. Full line width for each feature is from 0.6 to 3.4 km s⁻¹.

^d Time variation of the peak flux.

density. We find only small variations of the flux density of ICRF 0244+624 (~10%) and consider this scenario as unlikely.

Residual errors in the estimates of zenith delay corrections are much more likely. Since our observations were relatively short (~4 hr) and do not cover a large range of different elevations, it is difficult to separate the atmospheric and position offset contributions in the fringe phase. These residual errors can lead to position errors of several tens of microarcseconds for an individual observation. Since the atmospheric conditions between epochs are not correlated the resulting position errors are random.

A major problem in the parallax fitting is that most maser features show strong variability between the observations. Indeed, most features were not detected in all seven epochs. The flux densities of the maser features often change by up to a factor of 10, typically causing significant changes in the (blended) line shape and shifts in the apparent center velocity (Fig. 2). Since there is strong variability in blended spectra, one expects some effect on the astrometric accuracy of our measurements. Indeed, the fits yielded a spread in parallaxes with typical values between 0.45 and 0.55 mas, and a few outliers at 0.4 and 0.6 mas. This scatter in the parallax values is much larger than the formal

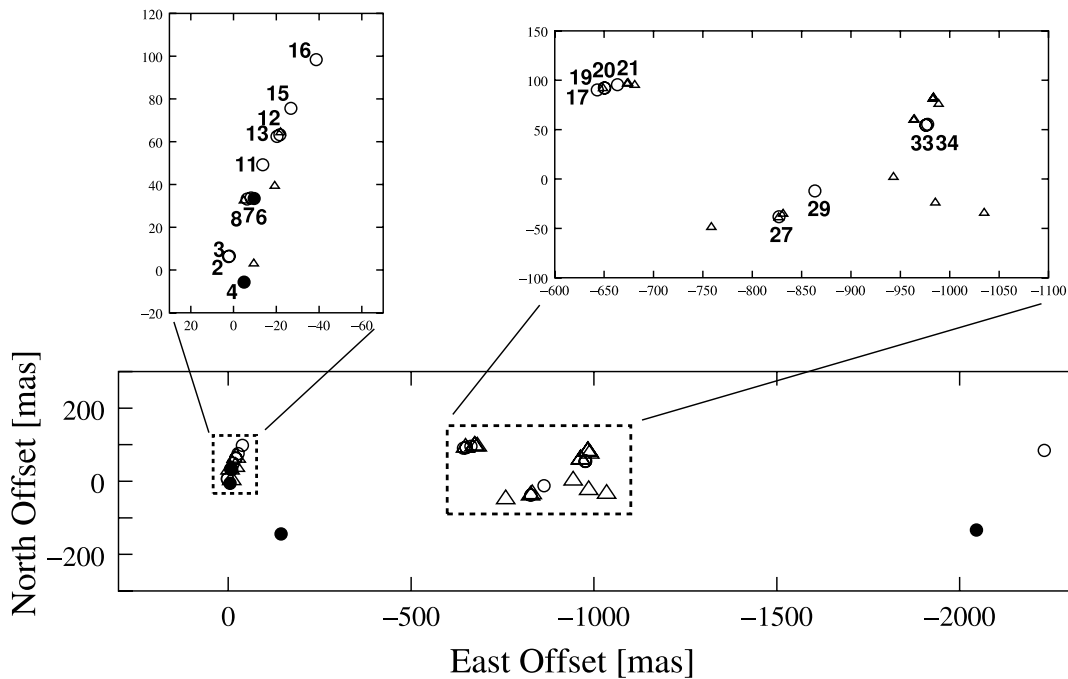


FIG. 1.—H₂O maser distribution. Filled circles show features detected in seven epochs, open circles show features detected in five or six epochs, and open triangles show features detected in three or four epochs. The numbers denote the components listed in Table 1 for which astrometrical fits were obtained.

accuracy. This scatter cannot be explained by the two previously mentioned sources of error (centroid position variation of the reference source and atmospheric contributions), since they affect all maser components similar.

For some components, the parallax model could not match the measured positions, as seen in reduced χ^2 values larger than ~ 3 . (In these cases, we probably are dealing with physical changes of the source, such as a brightening of one part of its only marginally resolved structure. Also, a new component with a similar radial velocity might appear at nearly the same position, while the existing one fades.) Other components had good fits, as evidenced by reduced χ^2 values near unity, but still showed a large scatter in the parallaxes. This can be explained by a correlation between the parallax and proper motion parameters, coupled with position errors caused by structural changes in some masers. Significant correlation coefficients are the result of nonoptimal time

sampling of position measurements, caused by telescope scheduling and maser variability. The effect of the nonoptimal time sampling is not identical for all maser components, because not all components were detected in all epochs.

The fits of most features show large correlation coefficients between the parallax and the proper motions. A histogram of the multiple correlation coefficient of the parallax clearly shows a bimodal distribution (Fig. 3)—with a few values below 0.3 and a large number with values larger than 0.4. Hence, we used only components that were detected in all seven epochs and showed a multiple correlation coefficient of the parallax parameter of < 0.3 . This left seven channels of component 1, which is the strongest and spectrally broadest of all features, and two channels of component 4. These components also had very symmetric spatial brightness distributions. The spectra of the two features in all seven epochs are shown in Figure 4. The parallaxes of the individual channel fits are in good agreement within their joint errors (Table 3).

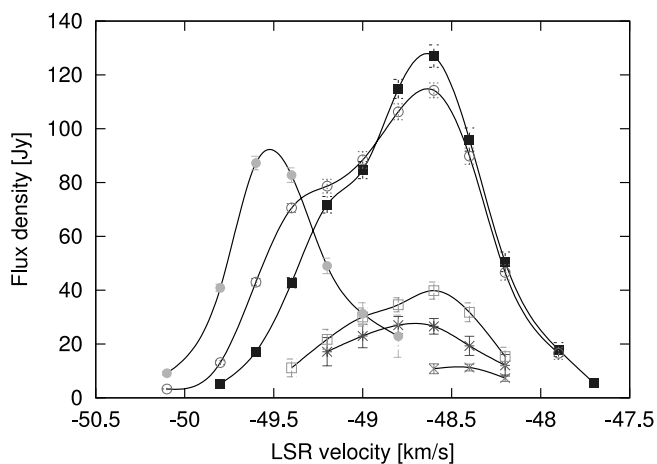


FIG. 2.—Spectra of component 7 at epoch 2 (*crosses*), epoch 3 (*stars*), epoch 4 (*open squares*), epoch 5 (*filled squares*), epoch 6 (*open circles*), and epoch 7 (*filled circles*). [See the electronic edition of the *Journal* for a color version of this figure.]

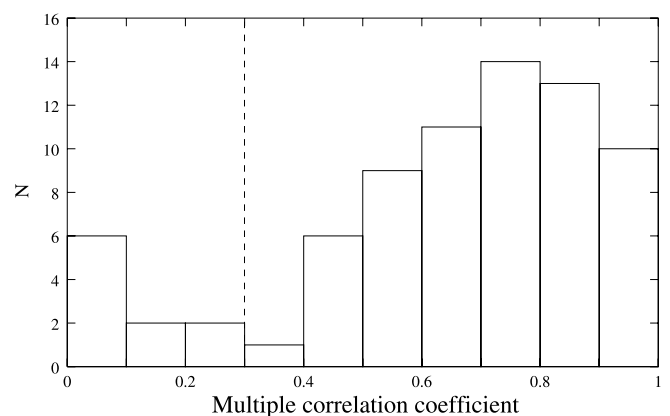


FIG. 3.—Histogram of the multiple correlation coefficients of the parallax parameter for different maser features. The dashed horizontal line marks the upper limit for the coefficient used to determine the final parallax.

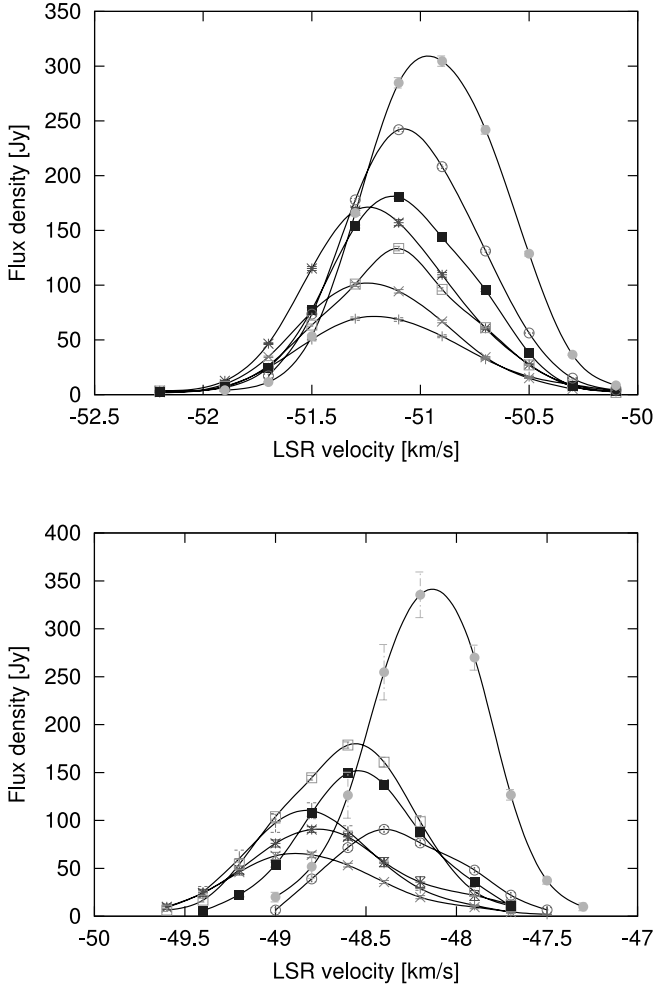


FIG. 4.—Spectra of components 1 (top) and 4 (bottom). See Fig. 3 for details. [See the electronic edition of the Journal for a color version of this figure.]

We also obtained a global fit to all nine channels with one parallax but allowing a different proper motion for each channel. The measured positions and our model for two channels are plotted in Figure 5. This global fit yields a parallax of 0.489 ± 0.009 mas. The 0.009 mas uncertainty is statistical only and does

TABLE 3
BEST-FIT ANNUAL PARALLAX FOR H₂O MASERS IN W3(OH)

Component	v_{LSR} (km s ⁻¹)	π (mas)
1.....	-50.3	0.516 ± 0.037
1.....	-50.5	0.479 ± 0.025
1.....	-50.7	0.489 ± 0.021
1.....	-50.9	0.494 ± 0.020
1.....	-51.1	0.497 ± 0.020
1.....	-51.3	0.490 ± 0.020
1.....	-51.5	0.482 ± 0.018
Average.....		0.492 ± 0.009
4.....	-48.2	0.465 ± 0.047
4.....	-48.4	0.486 ± 0.038
Average.....		0.476 ± 0.029
Global fit.....		0.489 ± 0.009

NOTE.—The errors of the annual parallaxes are from 20 to 50 μas for each spot, while the global fit shows 9 μas statistically.

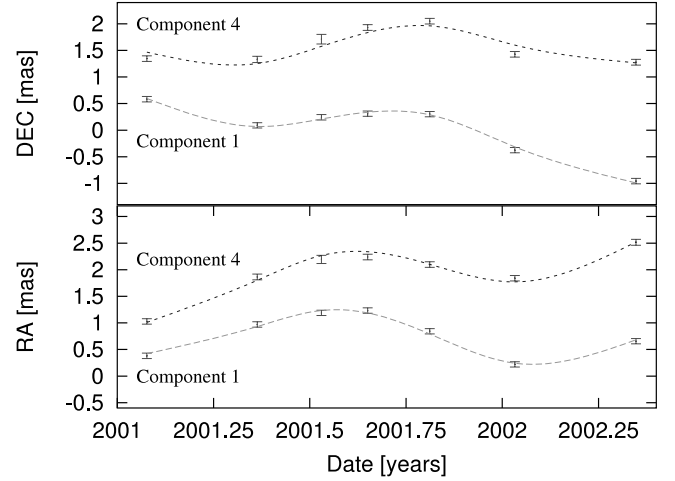


FIG. 5.—Positions vs. time for two maser components (V_{LSR} of -50.9 km s⁻¹ for component 1 and -48.4 km s⁻¹ for component 4) relative to the compact extragalactic source ICRF 0244+624. The top (bottom) plots show the northward (eastward) position components. Best-fit parallax and proper motions are indicated with dashed lines. [See the electronic edition of the Journal for a color version of this figure.]

not include systematic effects. Xu et al. (2006) see indications that parallax measurements might show some systematic sensitivity to the angular offset of the calibrators. For this effect, they included a systematic parallax error of about 0.007 mas deg⁻¹ of calibrator separation in their total uncertainty. This is probably caused by residual errors in the zenith delay correction. To be conservative, since ICRF 0244+624 has a separation from W3(OH) of $2''.2$, we add a systematic component of 0.015 mas to the statistical uncertainty of 0.009 mas. Therefore, we find the annual parallax of W3(OH)-TW to be $0.489 \pm 0.009 \pm 0.015$ mas, where the first error indicates the statistical error from the measurements while the second error describes a systematic atmospheric contribution.

To investigate this systematic error in more detail, we performed simulations in which we calculated the position offsets given a parallax (0.5 mas), random proper motions (between -4 and $+4$ mas yr⁻¹), position of W3(OH) on the sky, and dates of the observations. Then we added a random Gaussian error with an rms of $50 \mu\text{as}$ (the position accuracy of a single channel in a single epoch in our data) to each position offset and fitted the simulated data set. We fitted 1000 simulated data sets and found that the resulting parallaxes followed a Gaussian distribution with a standard deviation of ~ 0.015 mas. These errors also affect the proper motion fits. The difference between the true proper motion and the fitted proper motions in our simulations has a standard deviation of 0.04 mas yr⁻¹.

The annual parallax for W3(OH)-TW corresponds to a distance of $2.04 \pm 0.04 \pm 0.06$ kpc. This is far more accurate than any previous distance and comparable to the result of Xu et al. (2006). Photometric distance estimates of 2.2 kpc to an OB association near W3(OH) (Humphreys 1978) compare favorably with our value. However, the kinematic distance for a source at Galactic longitude $133^\circ 95'$ with an LSR velocity near -50 km s⁻¹ is 5 kpc. The reason for this large discrepancy is a peculiar motion of the W3(OH) region, which is discussed in detail in Xu et al. (2006).

3.2. Relative Maser Motions in W3(OH)-TW

The relative proper motions of the different maser features can be described by an outflow model. This has been successfully

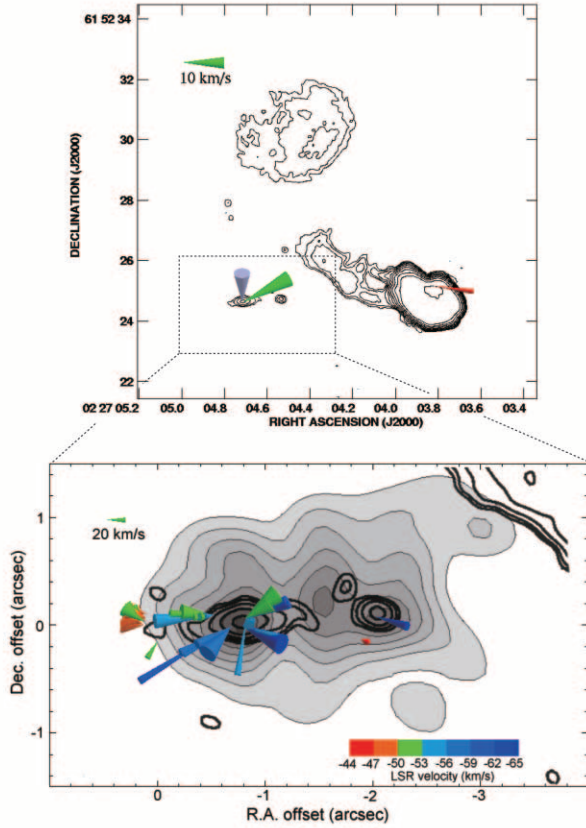


FIG. 6.—*Top*: The 8.4 GHz VLA continuum map of W3(OH) shown in contours (Wilner et al. 1999) with the absolute tangential motions of the TW object and the W3(OH) UC H II region indicated with cones. The colors indicate radial velocities as coded in the panel at the lower right. The gray cone shows their relative tangential motion. *Bottom*: The internal tangential motions of the W3(OH)-TW H₂O masers. The origin of the bottom figure is ($\alpha_{J2000} = 2^{\text{h}}27^{\text{m}}04^{\text{s}}.8362$, $\delta_{J2000} = 61^{\circ}52'24''.607$). The thin contours and gray scale represent the 220 GHz PdBI continuum map (Wyrowski et al. 1999). The peak positions for the TW object in this and the 8.4 GHz map are consistent with the expansion center of the outflow model.

applied to earlier VLBI observations of the H₂O masers in W3(OH) by Alcolea et al. (1993, hereafter A93). To estimate the physical parameters of the outflow model of W3(OH), we used the proper motions, radial velocities, and positions of maser features (Table 2). We chose component 1 from Table 2 as a reference feature and used its data to recalibrate all of the maser data. Component 1 was chosen because it is one of the strongest and least affected by blending of the masers (see § 3.1). We used only the maser features that were detected in at least three epochs. Figure 6 (*bottom panel*) shows the relative internal proper motions. We used the same method as A93, but we adopted our accurate distance of 2.04 kpc. We estimated the velocity and position of the center of expansion with respect to the reference maser feature and the expansion velocity V_{exp} at $1''$ from the center of expansion. Details of the model fitting are described in A93 and Imai et al. (2000). The best fit to the data was obtained minimizing the expression

$$\chi^2 = \sum \left[\left(\frac{u_x - W_x - v_x}{\sigma_x} \right)^2 + \left(\frac{u_y - W_y - v_y}{\sigma_y} \right)^2 \right] \quad (3)$$

$$\times \left[\left(\frac{u_z - W_z - v_z}{\sigma_z} \right)^2 \right], \quad (4)$$

TABLE 4
BEST-FIT MODEL FOR H₂O MASER VELOCITY FIELD

Parameter	Value
X_0	$-0''.89 \pm 0''.05$
Y_0	$0''.00 \pm 0''.03$
W_x	$-10.0 \pm 7 \text{ km s}^{-1}$
W_y	$16.0 \pm 7 \text{ km s}^{-1}$
V_{exp}	$13.0 \pm 5 \text{ km s}^{-1}$
α	-0.38 ± 0.2

where (u_x, u_y, u_z) are the motions of the maser feature in right ascension, declination, and the radial velocity, W_x and W_y are the tangential motions relative to the reference feature, and W_z is the radial velocity of the center of expansion. Parameters (v_x, v_y, v_z) are components of a maser spot's velocity, v , which is given by the equation of $\mathbf{v} = V_{\text{exp}} |\mathbf{r}|^\alpha \mathbf{r}/|\mathbf{r}|$ where $\mathbf{r} = (x - X_0, y - Y_0, z)$; $(\sigma_x, \sigma_y, \sigma_z)$ are components of the measurement uncertainty and a possible turbulent velocity of 4 km s^{-1} (added in quadrature). Finally, X_0 and Y_0 are the positions of the center of expansion relative to the phase-tracking center. We assigned a value of -51.0 km s^{-1} for the LSR velocity of the center of expansion (W_z), based on thermal molecular emissions from the location of the TW object (Wyrowski et al. 1997).

The results of the best model fit with a reduced χ^2 of 2.7 are shown in Table 4. The formal errors were increased by $\sqrt{2.7}$ to account for the χ^2 . It is not possible to compare the position of center of expansion between A93 and our results, since the A93 results were not phase-referenced. However, the parameter α agrees well with the value of A93. We find a value of $13.0 \pm 5 \text{ km s}^{-1}$ for the expansion velocity, which is slightly lower than the $20 \pm 2 \text{ km s}^{-1}$ value obtained by A93. This discrepancy is probably not significant, since A93 used a larger distance of 2.2 kpc that leads to larger velocities. When scaling the A93 results to our distance, one gets an expansion velocity of $18.5 \pm 2 \text{ km s}^{-1}$. Then the difference is $5.5 \pm 5.4 \text{ km s}^{-1}$.

In our case, the absolute position of the reference maser feature can be determined with respect to the extragalactic source and transferred to the other masers features and the center of expansion. Figure 6 displays the water masers and their tangential motions on the 8.4 GHz Very Large Array (VLA) continuum map of Wilner et al. (1999) and the 220 GHz Plateau de Bure interferometer (PdBI) continuum map of Wyrowski et al. (1999). Absolute positions of the TW object and the center of expansion of the H₂O maser outflow are listed in Table 5. The absolute position of center of expansion is consistent with the TW object, in which the H₂O maser outflow originates.

TABLE 5
ABSOLUTE POSITIONS OF THE CONTINUUM PEAK
AND THE H₂O MASER CENTER OF EXPANSION

Position	R.A. (J2000.0)	Decl. (J2000.0)
8.4 GHz.....	02 27 04.713	61 52 24.65
220 GHz.....	02 27 04.71	61 52 24.6
Center of expansion.....	02 27 04.7103±0.0071	61 52 24.607±0.030

NOTES.—Units of right ascension are hours, minutes, and seconds, and units of declination are degrees, arcminutes, and arcseconds. For the peak positions in the 8.4 and 220 GHz images we assume uncertainties of $0''.02$ and $0''.1$, typical for high-quality VLA and PdBI images. See text for the determination of the H₂O center of expansion uncertainty.

3.3. Relative Motion with Respect to the Ultracompact H II Region in W3(OH)

The tangential motion of the reference feature relative to the extragalactic background source ICRF 0244+624 obtained from the parallax/proper motion fit is $-1.2 \pm 0.5 \text{ km s}^{-1}$ eastward and $-10.2 \pm 0.5 \text{ km s}^{-1}$ northward, for a distance of 2.04 kpc. Adding the tangential motion of the center of expansion to these values gives the tangential motion of the center of expansion: $-11.2 \pm 7 \pm 0.4 \text{ km s}^{-1}$ eastward and $5.8 \pm 7 \pm 0.4 \text{ km s}^{-1}$ northward. The second error of 0.4 km s^{-1} comes from the systematics discussed in § 3.1. While this systematic error dominates the error in the parallax measurement, the fitting uncertainty of the outflow model dominated the total error in the proper motion of the center of expansion.

On the other hand, similar astrometric phase-referencing VLBA observations have been carried out for 12.2 GHz methanol masers associated with the UC H II region in W3(OH) (Xu et al. 2006). These authors have estimated the proper motion of these methanol masers with respect to extragalactic continuum sources and obtained a tangential motion of -11.1 ± 0.2 and $-1.3 \pm 0.1 \text{ km s}^{-1}$ eastward and northward, respectively. They have not estimated the internal motions of the methanol masers. However, these are approximately 2 km s^{-1} (Moscadelli et al. 2002), much smaller than the internal H₂O maser velocities. Thus, we assign a total uncertainty of 2 km s^{-1} to the absolute tangential motion of the methanol masers.

Combining the two VLBA results, the center of expansion of the H₂O masers (presumably the TW object) moves at $-0.1 \pm 7.3 \text{ km s}^{-1}$ eastward, $+7.1 \pm 7.3 \text{ km s}^{-1}$ northward, and -7 km s^{-1} in radial direction, with respect to the UC H II region of W3(OH). We used a systemic radial velocity of -51 km s^{-1} for the H₂O masers (TW object) and -44 km s^{-1} for the UC H II region in W3(OH). Converting this relative motion to a Galactic Cartesian coordinate system, the TW object relative to the UC H II region moves toward the Galactic center with a velocity of $7.3 \pm 5.9 \text{ km s}^{-1}$, in the direction opposed to Galactic rotation with $2.1 \pm 4.3 \text{ km s}^{-1}$ and toward the North Galactic Pole with $6.5 \pm 7.3 \text{ km s}^{-1}$.

4. DISCUSSION

4.1. Three-dimensional Dynamics and Structure of W3(OH)

In the case of W3(OH), a total (three-dimensional) motion of the TW object with respect to the UC H II region is $>7 \text{ km s}^{-1}$ (7 km s^{-1} in radial velocity plus $7 \pm 10 \text{ km s}^{-1}$ tangential motion). What causes this large relative motion? Assuming that the TW object and the UC H II region are gravitationally bound, a total mass (M_t) of the W3(OH) region can be estimated by

$$M_t \geq \frac{rv^2}{G} \quad (5)$$

$$\geq 1.1 \times 10^3 \left(\frac{r}{10^4 \text{ AU}} \right) \left(\frac{v}{10 \text{ km s}^{-1}} \right)^2 M_\odot, \quad (6)$$

where r is a separation of W3(OH)-TW and UC H II region and v is the relative motion. Since the separation along the line of sight is still unknown, a separation of 10^4 AU is a minimum value. This total mass is much higher than any reasonable estimate for the combined mass of the stars in W3(OH)-TW and the UC H II region, for which we estimate 17 and $23 M_\odot$, respectively, since the spectral type of the TW object is approximately B0 (Wyrowski et al. 1999) and that of the UC H II is approximately O8.5 (Harten 1976). So, these objects do not appear to be gravitationally bound.

The only other massive stars with similarly measured three-dimensional motions are the Becklin-Neugebauer object and radio source-I (related to IRc 2) in the Orion Kleinmann-Low region. The relative motion of these objects is very large, $>45 \text{ km s}^{-1}$ (Rodríguez et al. 2005), and Tan (2004) invokes ejection of the Becklin-Neugebauer object from the core of the Orion Nebula Trapezium cluster to explain this. However, for the W3(OH) sources, given their present-day relative motions, a close encounter of TW and the UC H II region could not have happened. Perhaps, one or the other (or both) had an encounter with a third object in the recent past and are now unbound.

4.2. Limitations of H₂O Maser Astrometry

The accuracy of the present H₂O maser parallax measurements achieved with phase-referencing VLBI is $\approx 10 \mu\text{as}$. However, the high time variability of H₂O masers limits such measurements in significant ways. While we detected over 40 maser features at any epoch and were able to trace 20 features over at least five epochs, only two of these 20 maser features had measurements that yield a reliable parallax measurement. In typical sources, few features might persist over a period of $\geq 1 \text{ yr}$, which is optimum for annual parallax measurements.

If one wishes to use the parallax and proper motion results to study Galactic structure and kinematics, one needs to model the internal motions of the masers. To obtain an accurate model fit of the internal motions, one needs to measure the motions of many maser features. Poor estimation of the internal motion (typical motions are $20\text{--}200 \text{ km s}^{-1}$) leads to inaccurate estimates of the three-dimensional motion. Of the many hundreds of known H₂O maser sources in the Milky Way, most will not have as many detectable components as W3(OH). Thus, it may be difficult to study Galactic dynamics using only H₂O masers.

Due to strong variability and large internal velocities, H₂O maser sources are not the best candidates to study the Galactic structure and dynamics. Other maser sources that show less variability and slower internal motions (e.g., methanol masers; Xu et al. 2006) are preferable. On the other hand, H₂O masers are much more common and also found in Galactic regions where no methanol masers are found. Some H₂O masers are found in the outer Galaxy near the edge of the optical stellar disk (e.g., Wouterloot et al. 1988), while methanol masers (e.g., Pestalozzi et al. 2005) have not been found there. Therefore, these H₂O masers can be the best sources to measure distances and motions in the outer Galaxy.

5. CONCLUSIONS

We have measured the annual parallax of the H₂O maser source in the W3(OH) region with phase-referenced VLBA observations. The distance of $2.04 \pm 0.07 \text{ kpc}$ that we obtain is consistent with previous photometric distance estimates (but with much higher accuracy) and with the CH₃OH maser parallax corresponding to $1.95 \pm 0.04 \text{ kpc}$ determined by Xu et al. (2006) in the related paper.

We also measured the proper motions of the W3(OH)-TW H₂O masers and find that the TW object is moving with a speed of $>7 \text{ km s}^{-1}$ with respect to the nearby UC H II region (with its OH and CH₃OH masers). Such a large speed difference between two massive objects in the same star-forming region is puzzling.

Although H₂O masers are not perfect target sources to investigate Galactic structure and dynamics, they can still provide important information about regions in the Galaxy that are not accessible otherwise (e.g., the outer Galaxy).

K. H. would like to thank the Japanese VLBI group for their assistance in preparing observations. K. H. would also like to thank J. M. Marcaide and J. C. Guirado at the University of València and E. Ros in MPIfR for advice in phase-referencing VLBI astrometry. We would like to thank F.

Wyrowski at MPIfR, who gave useful comments on the TW object. This work has been partially supported by the Spanish DGICYT grant AYA2002-00897. K. H. was partially supported by the Spanish Ministerio de Educación y Ciencia for his research.

REFERENCES

- Alcolea, J., Menten, K. M., Moran, J. M., & Reid, M. J. 1993, in *Astrophysical Masers*, ed. A. W. Clegg & G. E. Nedoluha (Heidelberg: Springer), 225
- Beasley, A. J., & Conway, J. E. 1995, in *ASP Conf. Ser. 82, Very Long Baseline Interferometry and the VLBA*, ed. J. A. Zensus, P. J. Diamond, & P. J. Napier (San Francisco: ASP), 328
- Briskin, W. F., Benson, J. M., & Goss, W. M. 2002, *ApJ*, 571, 906
- Brunthaler, A., Reid, M. J., & Falcke, H. 2005, in *ASP Conf. Ser. 340: Future Directions in High Resolution Astronomy*, ed. J. Romney & M. Reid (San Francisco: ASP), 455
- Chatterjee, S., Cordes, J. M., Vlemmings, W. H. T., Arzoumanian, Z., Goss, W. M., & Lazio, T. J. W. 2004, *ApJ*, 604, 339
- Fey, A. L., & Charlot, P. 2000, *ApJS*, 128, 17
- Harten, R. H. 1976, *A&A*, 46, 109
- Humphreys, R. M. 1978, *ApJS*, 38, 309
- Imai, H., Kameya, O., Sasao, T., Miyoshi, M., Deguchi, S., Horiuchi, S., & Asaki, Y. 2000, *ApJ*, 538, 751
- Kurayama, T., Sasao, T., & Kobayashi, H. 2005, *ApJ*, 627, L49
- Margon, B., & Kwitter, K. B. 1978, *ApJ*, 224, L43
- Moran, J. M., Papadopoulos, G. D., Burke, B. F., Lo, K. Y., Schwartz, P. R., & Thacker, D. L. 1973, *ApJ*, 185, 535
- Moscadelli, L., Menten, K. M., Walmsley, C. M., & Reid, M. J. 2002, *ApJ*, 564, 813
- Perryman, M. A. C., et al. 1995, *A&A*, 304, 69
- Pestalozzi, M. R., Minier, V., & Booth, R. S. 2005, *A&A*, 432, 737
- Reid, M. J., Argon, A. L., Masson, C. R., Menten, K. M., & Moran, J. M. 1995, *ApJ*, 443, 238
- Reid, M. J., & Brunthaler, A. 2004, *ApJ*, 616, 872
- Reid, M. J., Readhead, A. C. S., Vermeulen, R. C., & Treuhaft, R. N. 1999, *ApJ*, 524, 816
- Rodríguez, L. F., Poveda, A., Lizano, S., & Allen, C. 2005, *ApJ*, 627, L65
- Ros, E. 2005, in *ASP Conf. Ser. 340, Future Directions in High Resolution Astronomy*, ed. J. Romney & M. Reid (San Francisco: ASP), 482
- Smart, W. M. 1965, *Textbook on Spherical Astronomy* (5th ed.; Cambridge: Cambridge Univ. Press)
- Tan, J. C. 2004, *ApJ*, 607, L47
- Turner, J. L., & Welch, W. J. 1984, *ApJ*, 287, L81
- Valdettaro, R., et al. 2001, *A&A*, 368, 845
- van Langevelde, H. J., Vlemmings, W., Diamond, P. J., Baudry, A., & Beasley, A. J. 2000, *A&A*, 357, 945
- Vlemmings, W., van Langevelde, H. J., Diamond, P. J., Habing, H. J., & Schilizzi, R. T. 2003, *A&A*, 407, 213
- Wilner, D. J., Reid, M. J., & Menten, K. M. 1999, *ApJ*, 513, 775
- Wouterloot, J. G. A., Brand, J., & Fiegle, K. 1993, *A&AS*, 98, 589
- Wouterloot, J. G. A., Brand, J., & Henkel, C. 1988, *A&A*, 191, 323
- Wyrowski, F., Hofner, P., Schilke, P., Walmsley, C. M., Wilner, D. J., & Wink, J. E. 1997, *A&A*, 320, L17
- Wyrowski, F., Schilke, P., Walmsley, C. M., & Menten, K. M. 1999, *ApJ*, 514, L43
- Xu, Y., Reid, M. J., Zheng, X. W., & Menten, K. M. 2006, *Science*, 311, 54